



# The Role of Coagulation-Related Genes in Glioblastoma: A Comprehensive Analysis of the Tumor Microenvironment, Prognosis, and Treatment

Jingyi Yang<sup>1</sup> · Lei Shen<sup>1</sup> · Yuankun Cai<sup>1</sup> · Ji Wu<sup>1</sup> · Keyu Chen<sup>1</sup> · Dongyuan Xu<sup>1</sup> · Yu Lei<sup>1</sup> · Songshan Chai<sup>1</sup> · Nanxiang Xiong<sup>1</sup>

Received: 10 October 2024 / Accepted: 10 March 2025

© The Author(s), under exclusive licence to Springer Science+Business Media, LLC, part of Springer Nature 2025

## Abstract

The influence of coagulation on glioma biology has not been comprehensively elucidated. This study explores the role of coagulation-related genes (CRGs) in glioblastoma (GBM) from the perspectives of the tumor microenvironment (TME), differences in coagulation function among GBM patients, treatment, and prognosis. Somatic mutation analysis was performed on single nucleotide polymorphism (SNP) and copy number variation data from GBM patients in the TCGA cohort. Publicly available single-cell RNA sequencing data were used to analyze the role of coagulation in the GBM TME and its underlying biological mechanisms. Unsupervised clustering of GBM patients from the CGGA693 cohort was conducted, and coagulation function for each patient was assessed using ssGSEA scoring. Prognosis was assessed with Kaplan–Meier survival analysis, and immune infiltration was analyzed through ESTIMATE. A risk signature based on five CRGs (CFI, GNG12, MMP2, LEFTY2, and SERPINC1) was constructed and validated using LASSO regression and random survival forest analyses to predict responses to immunotherapy and identify potential sensitive drugs. Finally, the roles of LEFTY2 and SERPINC1 in GBM progression was verified by immunohistochemistry, cell counting kit-8 (CCK8) assay and wound healing assay, and the anti-GBM effect of the drug PLX4720 was verified by CCK8 assay, wound healing assay, and colony formation assay. Somatic mutation analysis revealed SNP events of CRG mutations in 117 out of 461 GBM cases (25.38%). Single-cell analysis of the GBM TME revealed significant activation of the coagulation pathway in endothelial cells, with intercellular communication mediated via the SPP1-integrin pathway ( $p < 0.01$ ). Clustering analysis and ssGSEA identified two coagulation-related subtypes in GBM: coagulation-activated and coagulation-inhibited subtypes. Patients in the coagulation-activated subtype exhibited shorter overall survival

---

Jingyi Yang and Lei Shen contributed equally.

---

Extended author information available on the last page of the article

and poorer prognosis compared to those in the coagulation-inhibited subtype ( $p=0.0085$ ). Immune infiltration analysis showed lower tumor purity and higher levels of immune-suppressive cells in the coagulation-activated subtype ( $p<0.001$ ). The CRG-based risk signature accurately predicted prognosis ( $p<0.0001$ ) and responses to immunotherapy in the IMvigor210 cohort ( $p=0.0062$ ). Based on the risk model, PLX4720 was identified as a potential sensitive drug ( $p<0.001$ ), and drug validation experiments demonstrated that PLX4720 inhibited the proliferation and migration of glioma cells ( $p<0.0001$ ). In vitro experiments demonstrated that LEFTY2 and SERPINC1 were significantly overexpressed in GBM compared to normal brain tissue, and knockdown of LEFTY2 and SERPINC1 inhibited glioma cell proliferation and migration ( $p<0.05$ ). The CRG-based risk signature model effectively predicts the prognosis of GBM patients and aids in assessing the efficacy of ICI therapy and chemotherapy. Furthermore, the genes LEFTY2, SERPINC1 and the drug PLX4720 offer potential directions for the development of novel therapeutic strategies for GBM.

**Keywords** Bioinformatic analysis · Coagulation · Glioblastoma · Machine learning · Prognosis · Tumor microenvironment

## Abbreviations

AC-like	Astrocyte-like GBM cell
CAF	Cancer-associated fibroblast
CGGA	Chinese Glioma Genome Atlas
CNV	Copy number variation
CRG	Coagulation-related gene
CR/PR	Complete response or partial response
CTRP	The Cancer Therapeutics Response Portal
DEGs	Differentially expressed genes
EC	Effector cells
ESTIMATE	The Estimation of STromal and Immune cells in MAlignant Tumor tissues using Expression data
GBM	Glioblastoma
GDSC	The Genomics of Drug Sensitivity in Cancer database
GEO	Gene Expression Omnibus database
GO	Gene ontology
GSVA	Gene set variation analysis
GSEA	Gene set enrichment analysis
GTEX	The Genotype-Tissue Expression Project
ICI	Immune checkpoint inhibitor
ICP	Immune checkpoint
IPS	Immunophenoscore
KEGG	Kyoto Encyclopedia of Genes and Genomes
LASSO	Least Absolute Shrinkage and Selection Operator
MES-like	Mesenchymal-like GBM cell
MGMT	O-6-Methylguanine-DNA Methyltransferase

---

MHC	Major histocompatibility complex molecules
NBT	Normal brain tissue
NC	Negative control
NES	Normalized enrichment score
NK	Natural killer
NPC-like	Neural progenitor-like GBM cell
OPC-like	Oligodendrocyte-progenitor-like GBM cell
OS	Overall survival
RNA-seq	RNA-sequencing
ROC	Receiver operating characteristic
SC	Suppressive cells
SD/PD	Stable disease or progressive disease
scRNA-seq	Single-cell RNA-sequencing
SNP	Single nucleotide polymorphism
ssGSEA	Single sample Gene Set Enrichment Analysis
SVM	Support vector machine
TCGA	The Cancer Genome Atlas
TF	Tissue factors
TIDE	Tumor immune dysfunction and exclusion
TME	Tumor microenvironment
TPM	Transcripts Per Kilobase of exon model per Million mapped reads

## Introduction

Glioblastoma (GBM) is one of the most aggressive primary brain tumors (Alexander and Cloughesy 2017). Due to its rapid progression and high recurrence rate, GBM patients face a grim prognosis, with a median survival of only 14 to 16 months (McKinnon et al. 2021). However, tumor heterogeneity and drug resistance limit the effectiveness of standard treatment approaches for GBM (Qazi et al. 2017). Therefore, there is an urgent need to develop new therapeutic approaches to enhance the survival outcomes of GBM patients (Rong et al. 2022; Khasraw et al. 2022).

Coagulation abnormalities are common clinical complications in cancer patients (Falanga et al. 2013, 2021). As a critical component of the vascular microenvironment, the coagulation system plays a vital role in shaping the tumor microenvironment (TME) in various cancers (Repetto and Re 2017; He et al. 2022; Saidak et al. 2021). Both *in vivo* and *in vitro* studies have demonstrated that a hypercoagulable state may promote immune evasion in tumors and impair the efficacy of immunotherapy (Bauer et al. 2022). Additionally, microvascular thrombotic occlusions contribute to hypoxia, pseudopalisading necrosis, and angiogenesis within the GBM TME, thereby driving malignant progression (Brat and Meir 2004; Tehrani et al. 2008; Prayson et al. 2011). Chronic activation of the coagulation system is particularly evident in GBM patients, with 30% experiencing venous thromboembolism and 92% developing microvascular thrombotic occlusions during the disease course (Yerrabothala et al. 2021; Magnus et al. 2013a). This hypercoagulable state not only increases the risk of thromboembolism but also

contributes to GBM growth and malignant progression by regulating intracellular signaling pathways related to coagulation (Magnus et al. 2013a, 2014). Studies have shown that the expression profiles of coagulation-related genes (CRGs) are closely associated with the molecular subtypes of GBM (Magnus et al. 2013b). However, the biological effects of coagulation in GBM remain to be elucidated.

The flow diagram of the bioinformatics analysis of this study is shown in Fig. 1. This study systematically investigates the oncological effects of coagulation in GBM and its underlying molecular mechanisms. We collected the single-cell RNA sequencing (scRNA-seq) dataset GSE141383 to investigate the interactions between coagulation and endothelial cells, exploring the biological mechanisms of thrombosis and coagulation in GBM. Using machine learning algorithms and comprehensive bioinformatics analyses, we identified two coagulation-related subtypes in GBM patients. Additionally, we examined the prognostic value of CRGs in GBM, constructed and validated a risk signature based on five key CRGs, and verified the roles of two newly identified CRGs in GBM through *in vitro* experiments. This study not only provides novel insights into the relationship between coagulation and the TME in GBM but also identifies potential biomarkers and therapeutic targets for personalized treatment, offering new avenues to improve patient prognosis.

## Materials and Methods

### Data Extraction of Public GBM Cohorts

RNA-seq profiles and the corresponding clinical data of GBM patients were obtained from the UCSC Xena database (<https://xenabrowser.net/>) and CGGA database, including 141 GBM samples from TCGA and 388 GBM samples from CGGA. The clinical characteristics of GBM patients included in this study were summarized in Table 1. Specifically, GBM patients in CGGA693 were assigned to the training set, while patients in CGGA325 and TCGA were assigned to the

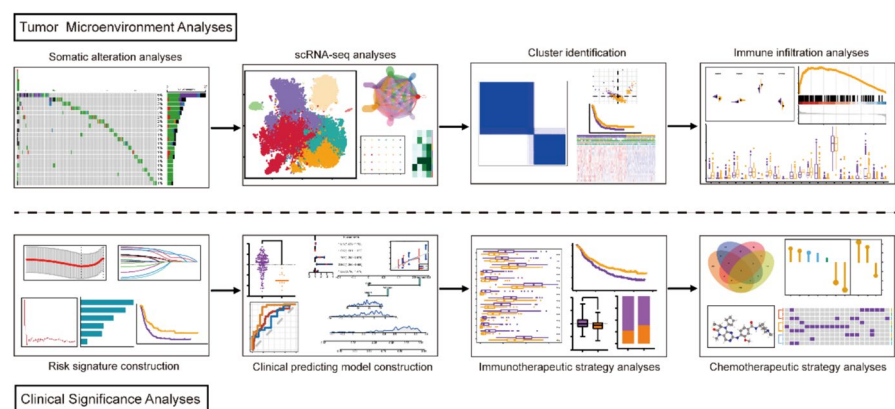


**Fig. 1** Flow diagram of the bioinformatics analysis

**Table 1** Clinical characteristics of GBM patients in the public cohorts

Clinical characteristics	CGGA693 (n=249)	TCGA (n=141 <sup>#</sup> )	CGGA325 (n=139)
Age			
>50	119	109	60
≤50	130	32	79
Gender			
Male	147	93	88
Female	102	48	51
<i>IDH</i> Mutation status			
Mutant	49	10	41
Wildtype	190	128	98
NA	10	3	0
1p/19q Co-deletion status			
Codel	13	0	7
Noncodel	205	133	129
NA	31	8	3
MGMT promoter methylation status			
Unmethylated	93	66	70
Methylated	106	45	66
NA	50	30	3

*IDH* isocitrate dehydrogenase, *MGMT* O-6-Methylguanine-DNA Methyltransferase, NA not available

<sup>#</sup>The TCGA cohort in the table refers to the GBM patients with RNA-seq data

validation sets for subsequent analyses. All the RNA-seq data in this study were converted to Transcripts Per Kilobase of exon model per Million mapped reads (TPM) for further analysis.

### Somatic Alteration Analysis

Single nucleotide polymorphism (SNP) and copy number variation (CNV) data of GBM patients in TCGA were retrieved from the UCSC Xena database. We selected the top six SNP events, including missense mutation, nonsense mutation, splice site, frame shift deletion, frame shift insertion, and multi-hit. The copy number value of each gene was normalized and estimated using GISTIC2 (<https://broadinstitute.github.io/gistic2/>) (Mermel et al. 2011). A gene was defined as having a copy number gain if the copy number value of this gene exceeded 0.3, and a copy number loss if it was below 0.3. We further analyzed the association between the overall survival (OS) and the CNV status of CRGs.

## Analysis of scRNA-seq Data

To explore the role of coagulation in the TME of GBM, we collected the scRNA-seq dataset GSE141383 from the Gene Expression Omnibus (GEO) database (Chen et al. 2021). The scRNA-seq data were normalized and analyzed using the R package “Seurat” (Satija et al. 2015). R package “Harmony” was used to integrate the scRNA-seq data and eliminate the batch effect (Korsunsky et al. 2019). Four widely used GBM subtypes—neural progenitor-like (NPC-like), oligodendrocyte-progenitor-like (OPC-like), astrocyte-like (AC-like), and mesenchymal-like (MES-like)—based on scRNA-seq data were used for cell type annotation (Neftel et al. 2019). Enrichment analysis at the scRNA-seq level was performed by R package “irGSEA” (<https://github.com/chuiqin/irGSEA>), which integrated the AUCell (Aibar et al. 2017), UCell (Andreatta and Carmona 2021), singscore (Foroutan et al. 2018) and ssGSEA via the robust rank aggregation algorithm in the R package “RobustRankAggreg” (Kolde et al. 2012). The cell–cell communications and interactions were analyzed using R package “cellchat” (Jin et al. 2021).

## Machine Learning Algorithms to Identify Coagulation-Related Subtypes

The coagulation pathway (HALLMARK\_COAGULATION) was obtained from the MSigDB (<https://www.gsea-msigdb.org/gsea/msigdb/>) (Liberzon et al. 2015). A total of 138 genes in the pathway were considered CRGs. Consensus clustering (Wilkerson and ConsensusClusterPlus 2010) and K-Means clustering algorithms were applied to identify coagulation-related subtypes based on CRG expression in GBM patients from the CGGA693 dataset. The support vector machine (SVM) algorithm, implemented through the R package ‘e1071’ (<https://cran.r-project.org/web/packages/e1071/>), was used to learn the characteristics of different coagulation-related subtypes and assign them to the validation sets. Principal component analysis (PCA) was performed to visualize the differences between subtypes. The R package “gene set variation analysis” (GSVA) was used to perform the single-sample gene set enrichment analysis (ssGSEA) (Hanzelmann et al. 2013).

## Identification of Differentially Expressed Genes

To reduce the false positive rate of discovering differentially expressed genes (DEGs), we employed the Wilcoxon rank-sum test and multiple hypothesis testing to identify DEGs (Li et al. 2022). The p-values of the Wilcoxon rank-sum test were adjusted to the false discovery rate (FDR) by the Benjamini–Hochberg method. The fold change was calculated using the average gene expression of each group. Genes with FDR less than 0.05 and |Log2 (Fold Change)| greater than 1 were regarded as DEGs.

## Immune Infiltration Analysis for Different Subtypes

The Estimation of STromal and Immune cells in MAlignant Tumor tissues using Expression data analysis (ESTIMATE) was conducted to estimate the tumor purity in each sample (Yoshihara et al. 2013). Considering four major categories of genes — effector cells (EC), suppressive cells (SC), major histocompatibility complex molecules (MHC), and immune checkpoint (ICP) — we estimated the immunophenoscore (IPS) by R package “Immunophenogram” (<https://github.com/icbi-lab/Immunophenogram>), which reflects the tumor immunogenicity. Gene set enrichment analysis (GSEA) (Subramanian et al. 2005) and GSVA were used to identify immune-related pathways enriched in different subtypes, based on the Kyoto Encyclopedia of Genes and Genomes (KEGG) (Kanehisa et al. 2021) and Gene Ontology (GO) (Aleksander et al. 2023). The immune cell infiltration of each sample was analyzed with CIBERSORT (Newman et al. 2015).

## Construction of CRG-Based Risk Signature and Nomogram

207 normal brain tissues (NBT) were obtained from Genotype-Tissue Expression Project (GTEx) for comparison (GTEx Consortium 2013). Differentially expressed (DE) CRGs identified between NBT and GBM were further screened. Univariate Cox regression was used to select the prognostic DE CRGs. The least absolute shrinkage and selection operator (LASSO) analysis (Tibshirani 1997) and co-linearity analysis were conducted to screen valuable CRGs. To filter out the most valuable CRGs, we further performed random survival forest analysis (Taylor 2011), a machine learning algorithm, based on the LASSO results. The variable relative importance cut-off in random survival forests was set to 0.3. The multivariate Cox regression was conducted to construct the risk signatures based on the screened DE CRGs. The risk scores were calculated using the following algorithm: Risk Score = coefficient of Gene1 \* expGene1 + coefficient of Gene2 \* expGene2 + ... + coefficient of GeneN \* expGeneN. In this formula, the coefficient represents the regression coefficient of genes obtained from multivariate Cox regression analysis, and ‘exp’ denotes the expression levels of the corresponding genes. According to the risk scores and cut-off value, patients were divided into high- and low-risk groups. To enhance predictive performance of the risk signature, a clinical prediction model was constructed based on the risk score and clinical characteristics. R package "regplot" (<https://cran.r-project.org/web/packages/regplot/>) was used to build and visualize the nomogram. The performance of the prediction model was assessed using receiver operating characteristic (ROC) curves and the area under the curve (AUC). Additionally, the performance of the nomogram was evaluated using calibration curves.

## Evaluating the Predictive Abilities of the Risk Signature for the Treatment Efficacy of ICI Therapy

Tumor Immune Dysfunction and Exclusion (TIDE) method was applied to predict the immunotherapy response (Jiang et al. 2018). Three immunotherapy cohorts,

including IMvigor210 (Necchi et al. 2017), GSE135222 (Jung et al. 2019), and GSE78220 (Hugo et al. 2016), were collected to evaluate the predictive abilities for immunotherapy efficacy. IMvigor210 cohort contains the RNA-seq data and clinical data of patients with metastatic urothelial cancer treated with anti-PD-L1 checkpoint inhibition therapy. GSE135222 is a cohort of lung cancer patients treated with anti-PD-1/PD-L1 therapy. GSE78220 is a melanoma cohort of patients treated with anti-PD-1 checkpoint inhibition therapy. Based on the response to ICI treatment, patients were categorized into two groups, stable disease or progressive disease (SD/PD) and complete response or partial response (CR/PR).

### Potential Small Molecular Drugs Prediction

The sensitivity to small molecular drugs was assessed using the R package ‘oncoPredict’ based on drug sensitivity data and expression data (Maeser et al. 2021). The drug sensitivity data and expression data were obtained from the Genomics of Drug Sensitivity in Cancer (GDSC) database (Yang et al. 2013), the Cancer Therapeutics Response Portal (CTRP) (Rees et al. 2016), and the Cancer Cell Line Encyclopedia (Barretina et al. 2012). Drug sensitivity was assessed by a sensitivity score, with a lower score indicating higher sensitivity to potential drugs. SwissTargetPrediction (Gfeller et al. 2013), SuperPred (Nickel et al. 2014), and similarity ensemble approach (SEA) (Keiser et al. 2007) were used as reliable tools to predict the targets of small molecular drugs. After identifying the potential drugs, the possible interactions between CRGs and the potential drugs were estimated utilizing these tools. The 3D structures of the potential drugs were obtained from PubChem (Kim et al. 2021).

### Frozen Sections and Immunohistochemistry Staining

Three GBM and three NBT tissue samples were collected from Zhongnan Hospital of Wuhan University for immunohistochemistry. These tissues were quickly frozen in liquid nitrogen and subsequently dehydrated using a 15–30% gradient sucrose solution. The tissues were embedded on a sample tray using an optimal cutting temperature compound embedding agent and frozen until solidified in a –22 °C freezer of a frozen sectioning machine. Trimming was performed to expose the largest section. The slice thickness was adjusted to 8 µm and performed frozen sections. After sectioning, the samples were fixed with formaldehyde for 30–60 s to preserve tissue morphology. Immunohistochemical staining of tissue sections was performed using the Mouse and Rabbit Specific HRP/AEC IHC Detection Kit (#ab236467, Abcam, Shanghai China) following the manufacturer’s instructions. The following antibodies were used: LEFTY2 (#13991-1-AP, Proteintech, Wuhan China), SERPINCl (#A11249, ABclonal, Wuhan China). Tissue samples were obtained and used with the approval of the Medical Ethics Committee of Zhongnan Hospital of Wuhan University (Ethical Approval No. 2021080).

## Cell Culture and Transfection

Glioma cell lines, A172 and U251, were obtained from the Chinese Academy of Sciences Cell Bank (Shanghai China). The cells were cultured in Dulbecco's modified Eagle medium (DMEM) (#G4511, Servicebio, Wuhan China) containing 10% fetal bovine serum (FBS) (#FBS500-H, Hycezbio, Wuhan China) and 10  $\mu$ l/ml penicillin–streptomycin (#BL505A, Biosharp, Guangzhou China) and incubated in a humidified chamber at 37 °C with 5% CO<sub>2</sub>.

The transfection procedure was as follows. First, 100,000 glioma cells were inoculated into each well of a 6-well plate and cultured overnight in DMEM containing 10% FBS and 10  $\mu$ l/ml penicillin–streptomycin. After reaching 60–70% confluence, cells with optimal morphology were transfected with 10 nM of LEFTY2-siRNA and SERPINC1-siRNA (designed and manufactured by GeneChem Biotech, Shanghai China) and 6  $\mu$ l/ml RNATransMate (#E607402, sangon biotech, Shanghai China) in serum-free complete medium. Next, the cells were cultured at 37 °C in a 5% CO<sub>2</sub> humidified incubator for 8 h. After 8 h of transfection, the medium was changed to DMEM containing 10% FBS, 10  $\mu$ l/ml penicillin–streptomycin. The sequence of LEFTY2-siRNA was as follows: sense, 5'-GGCGACUGUGA CCCUGAACG-3' and anti-sense, 5'-UUCAGGGUCACAGUCGCCUG-3'. The sequence of SERPINC1-siRNA was as follows: sense, 5'-AUCACAUUGGAAUAC AUGGCC-3' and anti-sense, 5'-CCAUGUAUCCAAUUGUGAUAG-3'.

## RNA Extraction and Real-Time Quantitative PCR (qPCR)

Total RNA was extracted from cells using Takara RNAiso Plus (#9109, Takara Bio, Japan). cDNA was synthesized from 250 ng RNA using the HiScript III 1st Strand cDNA Synthesis Kit (+gDNA wiper) (#R312-01, Vazyme Biotech, Nanjing China). QPCR was performed with ChamQ SYBR qPCR Master Mix (#Q341-02, Vazyme Biotech) and Rotor-Gene Q real-time PCR instrument (Qiagen, Germany) in triplicate. The relative levels of LEFTY2 and SERPINC1 were normalized by ACTB. The amplification efficiencies of these three primers, ACTB, LEFTY2 and SERPINC1, were 95.0%, 102.4% and 105.2%, respectively. All data were calculated using the  $2 - \Delta\Delta Ct$  method. The primer sequences were: ACTB forward, 5'- AGC AGTCGGTTGGAGCGAGCAT -3'; ACTB reverse, 5'- TGGCTTTGGGAGGG CAAGGGA -3'; LEFTY2 forward, 5'-TGGACCTCAGGGACTATGGAG-3'; LEFTY2 reverse, 5'-CCGAGGCGATACACTGTCG-3'; SERPINC1 forward, 5'- ACTGAAGTGGCGACTCTATCG-3'; SERPINC1 reverse, 5'- GGCTCCATATAC CAACTCACTGA-3'.

## Cell Counting Kit-8 (CCK-8) Assay, Wound Healing Assay and Colony Formation Assay

After transfecting cells with siRNA and its control, cell viability was assessed using the CCK-8 assay kit (#A311-01, Vazyme Biotech). In each experiment, knockdown

efficiency was tested in cells cultured simultaneously to ensure the accuracy of the experimental results. Firstly, A172 and U251 cells were seeded at a density of 5,000 cells/100 µl/well and cultured in 96-well plates for 48 h. Subsequently, 10 µl of CCK-8 solution was added to each well and incubated for 2 h at 37 °C. Finally, the optical density (OD) value was measured at 450 nm by using a BioTek Synergy HT Microplate Reader. Since the OD value was linearly related to the number of cells, we used the OD value to estimate the effect of transfected siRNA on the proliferation ability of glioma cells. Graph Pad Prism was used to conduct statistical analysis and generate the charts.

The wound healing assay was performed to evaluate cell migration ability. A172 and U251 cells were seeded in 6-well plates at a density of 500,000 cells/1 ml/well in 10% FBS medium. When 90–100% confluence was reached after 24 h, 10 µl disposable pipette tips were used to create wounds by scratching the cell monolayer. The cells were washed three times with phosphate buffered saline (PBS) (#G4202, Servicebio) and 10% FBS medium was replaced with 3% FBS (low concentration) medium. The purpose of culturing in 3% FBS medium is to sustain cell survival while minimizing the effects of proliferation on the results. The extent of wound healing was measured at 0 and 48 h under an optical microscope.

In the colony formation assay, A172 and U251 cells were seeded in 6-well plates at a density of 200 cells/well, and the experiments were performed in triplicate. After 14 days of incubation, when colony formation was visible to the naked eye and the number of cells per colony was greater than 50 under the microscope, the plates were washed twice with PBS, fixed with 4% paraformaldehyde (#G1101, Servicebio) for 30 min, and stained with 0.1% crystalline violet solution (#G1014, Servicebio) for 15 min. Photographs were then taken to determine the number of colonies for analysis.

## Drug Validation Experiments

We performed CCK8 assay, wound healing assay, and colony formation assay to assess the effect of potential drug PLX4720 on glioma cells. PLX4720 was purchased from MedChemExpress (HY-51424, New Jersey, USA). A172 and U251 cells were cultured in normal complete medium without or with PLX4720 at concentrations of 0.5 µM, 1 µM, 2 µM, 4 µM, 8 µM, and 16 µM, respectively, for 24 h. The OD values were measured and GraphPad Prism (version 9.0.0, GraphPad Software, Boston, USA) was used to analyze the OD values for dose-response curves and calculate the IC<sub>50</sub>. The cell survival rate was calculated using the following formula: cell survival rate = [(As – Ab)/(Ac – Ab)] × 100%, where As is the OD value of the dosing group, Ac is the OD value of the non-dosing group, and Ab is the OD value of the blank group.

A172 and U251 cells at a density of 5,000 cells/100 µl/well were cultured in normal complete medium and complete medium containing PLX4720 at a concentration of 6 µM for 24, 48 and 72 h, respectively. The cell proliferation curves were analyzed by GraphPad Prism using the OD values. Cell viability was

calculated using the formula described above, where As is the OD value at 24, 48, or 72 h, Ac is the OD value at 0 h, and Ab is the OD value of the blank group.

Normal complete medium or medium containing 6  $\mu$ M PLX4720 was added to A172 and U251 cells immediately after wounding. Photographs were taken under an optical microscope at 0 h and 48 h, and the wound area was measured using ImageJ (National Institutes of Health, Maryland, USA). The wound healing rate was calculated using the following formula: wound healing rate = (Area 0 h—Area 48 h)/Area 0 h.

In colony formation assays, A172 and U251 cells at a density of 200 cells/well were cultured for 14 days in normal complete medium or medium containing 6  $\mu$ M PLX4720. The colonies were photographed, counted, and analyzed using GraphPad Prism to evaluate the effect of PLX4720 on the proliferative capacity of glioma cells.

## Statistical Analysis

Statistical analyses and data visualizations were performed using R (version 4.3.0) and GraphPad Prism (version 9.0.0). Spearman correlation analysis was used to evaluate the correlation between data. Shapiro–Wilk test was used to assess the normality of the data. The Student’s t-test was used to compare differences in continuous variables between two normally distributed datasets. The Wilcoxon rank-sum test was used to compare continuous variables between non-normally distributed datasets. The Chi-square test was used to compare the differences between two groups of discrete random variables. Kaplan–Meier analysis was used to compare survival outcomes between the two groups. Two-sided  $p \leq 0.05$  (\*) was considered statistically significant and categorized as  $p < 0.01$  (\*\*),  $p < 0.001$  (\*\*\*), and  $p < 0.0001$  (\*\*\*\*).

## Results

### Somatic Alteration Landscape of CRGs

To explore the genomic features of CRGs in GBM, we visualized the mutation frequency of CRGs in 461 GBM patients in the TCGA cohort (Fig. 2A). The SNP events of CRGs occurred in 25.38% of GBM patients, with mutation frequencies ranging from 1 to 7%. The most frequent SNP event was the missense mutation. The CRGs with the highest mutation frequency were LRP1 (6%), VWF (3%), and TMPRSS6 (3%). The lollipop chart showed the CNV frequency of the top 20 CRGs (Fig. 2B). CNV losses occurred more frequently than CNV gains in CRGs in GBM patients. The top 5 CRGs with the highest CNV loss incidence were KLK8 (11.46%), MASP2 (10.35%), CPB2 (9.08%), APOC1 (8.76%), and APOC2 (8.76%). Meanwhile, the top 5 CRGs with the highest CNV gain incidence were HRG (4.30%), F10 (4.14%), PROZ (4.14%), CFD (3.98%), and LRP1 (3.66%) (Supplementary file 1). The CNV status of CRGs was also correlated with the prognosis of GBM patients. GBM Patients with CNV gains or losses of ADAM9, CTSK,

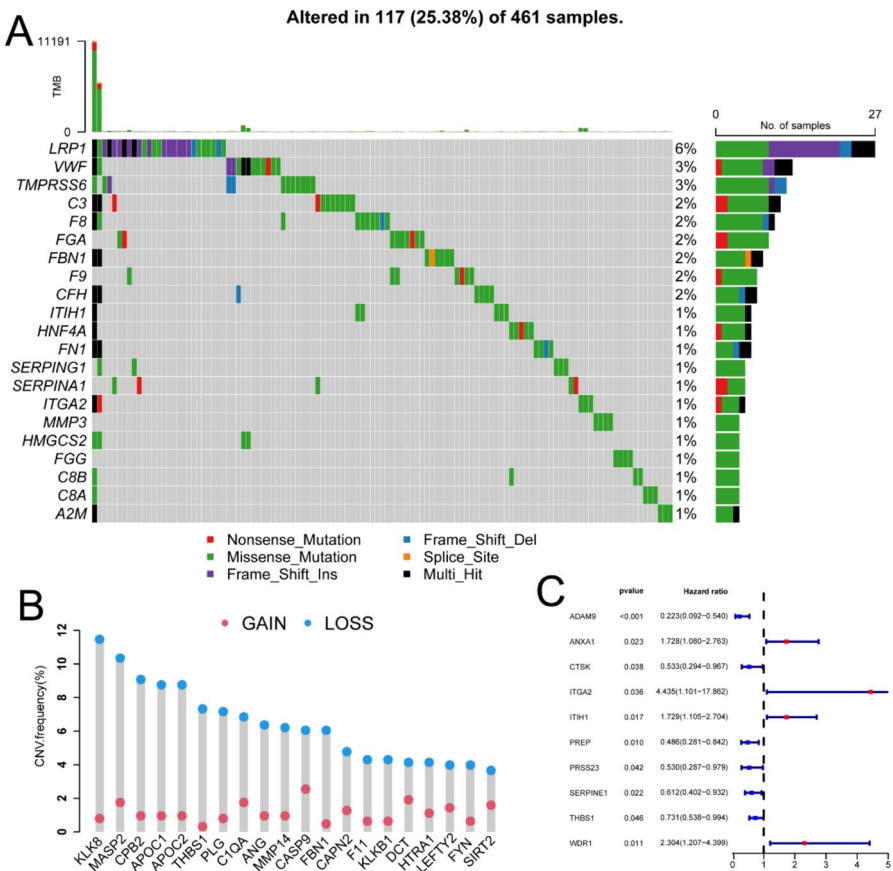


**Fig. 2** Somatic alteration landscape of GBM. **A**, oncplot of the top 20 CRGs' SNPs in GBM. **B**, lollipop chart of the top 20 CRGs' CNVs in GBM. **C**, forest plot of the top 10 CRGs in GBM. *CRG* coagulation-related gene, *SNP* single nucleotide polymorphism, *CNV* copy number variation

PREP, PRSS23, SERPINE1, and THBS1 had better prognoses, while those with CNV gains or losses of ANXA1, ITGA2, ITIH1, and WDR1 had worse prognoses (Fig. 2C).

### Cross-Talking Between GBM Cells and Endothelial Cells Based on the scRNA-seq Data

Using scRNA-seq data, we further elucidated the role of coagulation in the TME of GBM. T-distributed Stochastic Neighbor Embedding (t-SNE) dimension reduction was performed on 29,415 cells from 9 GBM samples, resulting in 16 clusters and 7 cell types (Fig. 3A). Cluster cell types were identified based on the expression of known marker genes and visualized in the dot plot (Fig. 3B, Supplementary file 2). The irGSEA results showed that the coagulation pathway was enriched

in endothelial cells, AC-like GBM cells, macrophages, and MES-like GBM cells (Fig. 3C). According to the AUCell score distribution, the coagulation pathway was most prominently enriched in endothelial cells, followed by MES-like GBM cells (Fig. 3D).

Moreover, we inferred the communication between endothelial cells and other cells in the TME of GBM to explore the oncological effect and mechanisms of coagulation. The communication networks showed the quantity and intensity of interactions between different cell types (Fig. 4A). As shown in the network, the endothelial cells had communications with all other cell types (Fig. 4B). According to our findings, endothelial cells received signals from cancer-associated fibroblasts, macrophages, AC-like GBM cells, OPC-like GBM cells, NPC-like GBM cells, and MES-like GBM cells through the SPP1-integrin signaling pathway ( $p < 0.01$ ) (Fig. 4C). The matrix heatmap demonstrated the significant correlation between the ssGSEA score of coagulation and the expression of receptors and ligands in the SPP1-integrin signaling pathway (Fig. 4D). Through systematic analysis of the communication network, which combines the signal strength of SPP1-integrin transmitted and received by each cell type, we identified the roles of different cell types in the SPP1-integrin signaling pathway in GBM.

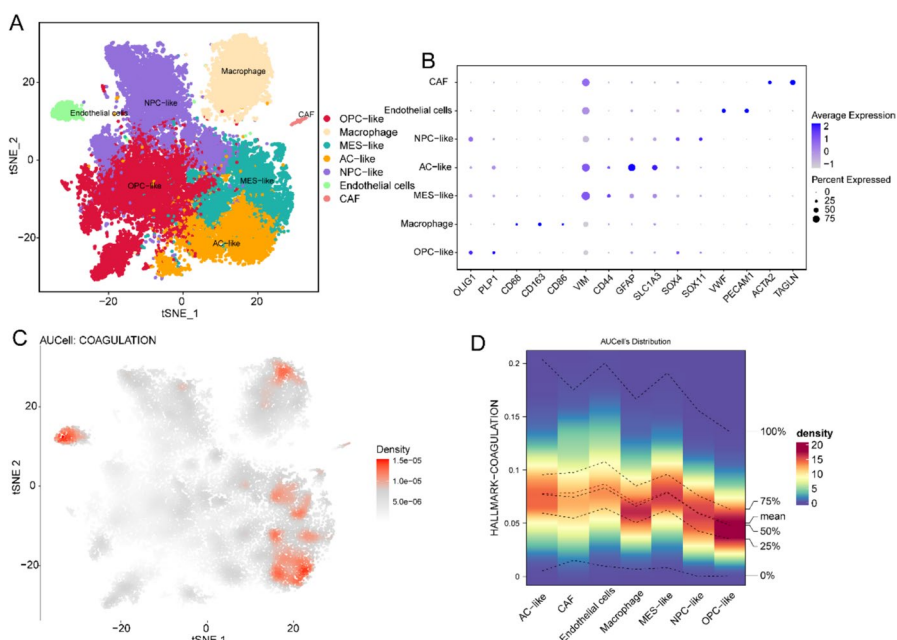


**Fig. 3** Investigation of the role of coagulation in TME of GBM using scRNA-seq analyses. **A**, t-SNE plot of the TME in GBM. **B**, expression of marker genes for different cell types. **C**, distribution of coagulation scores in TME of GBM. **D**, distribution of coagulation scores in different cell types. *TME* tumor microenvironment, *AC-like* astrocyte-like GBM cell, *MES-like* mesenchymal-like GBM cell, *NPC-like* neural progenitor-like GBM cell, *OPC-like* oligodendrocyte-progenitor-like GBM cell, *CAF* cancer-associated fibroblast

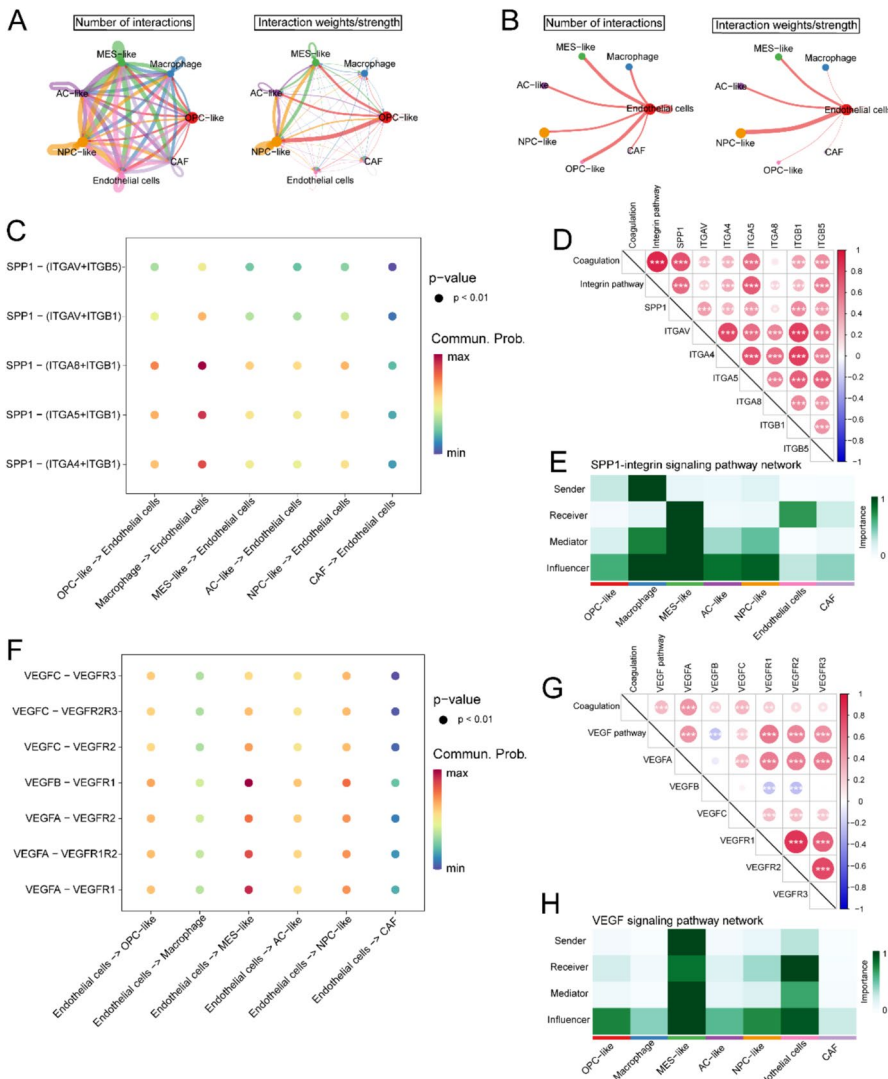


**Fig. 4** Cell–cell communication analyses **A**, overview of cell–cell communication between different cell types. **B**, overview of cell–cell communication between endothelial cells and other cells. **C**, likelihood of communication via the SPP1-integrin pathway from other cells to endothelial cells. **D**, correlation between coagulation scores and the SPP1-integrin pathway in bulk RNA-seq data. **E**, the SPP1-integrin signaling pathway network showed endothelial cells are likely the receiver. **F–H**, communication from endothelial cells to other cells via the VEGF pathway

Macrophages were identified as senders, while endothelial cells and MES-like GBM cells were detected as receivers (Fig. 4E). In addition, endothelial cells also sent signals via the VEGF signaling pathway to other cells ( $p < 0.01$ ) (Fig. 4F).

The correlation analysis and the communication network systematic analysis also confirmed this finding (Fig. 4G, H).

### Identification of Coagulation-Related GBM Subtypes

Based on the expression of CRGs from the CGGA693 dataset, two coagulation-related subtypes were identified using the unsupervised clustering method (Fig. 5A). All patients were divided into two groups according to the PCA results, further confirming two remarkably different subtypes related to coagulation (Fig. 5B). We found that subtype 1 had a higher ssGSEA score of coagulation ( $p < 0.0001$ ) and

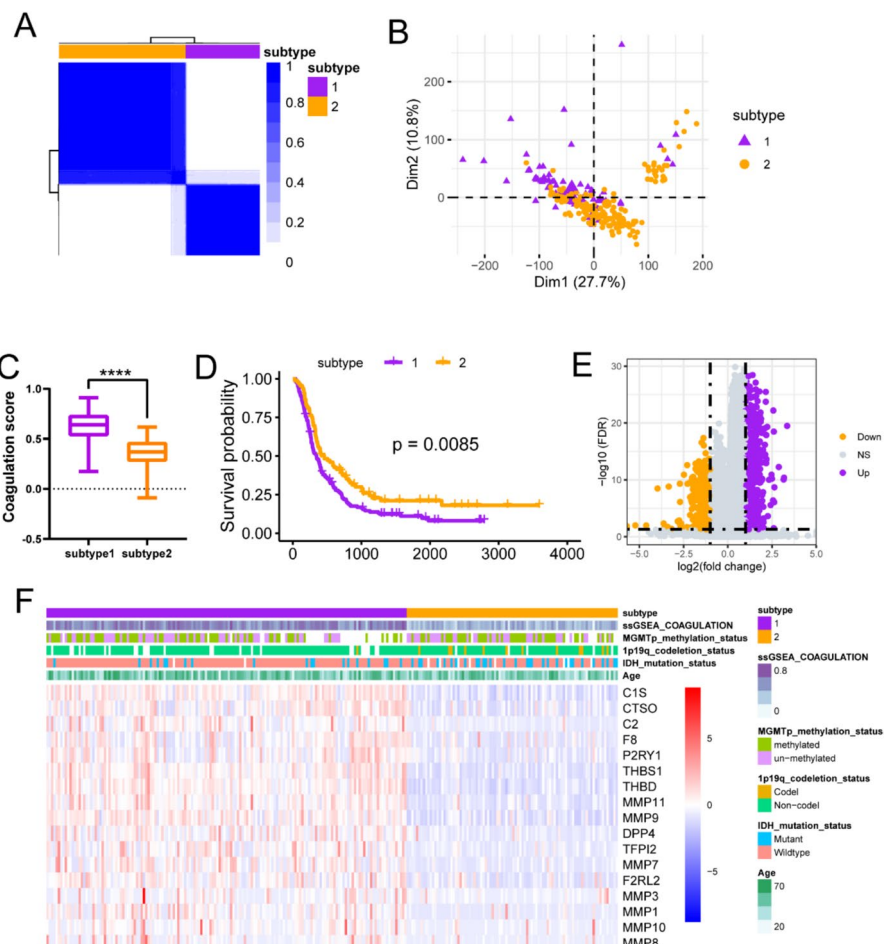


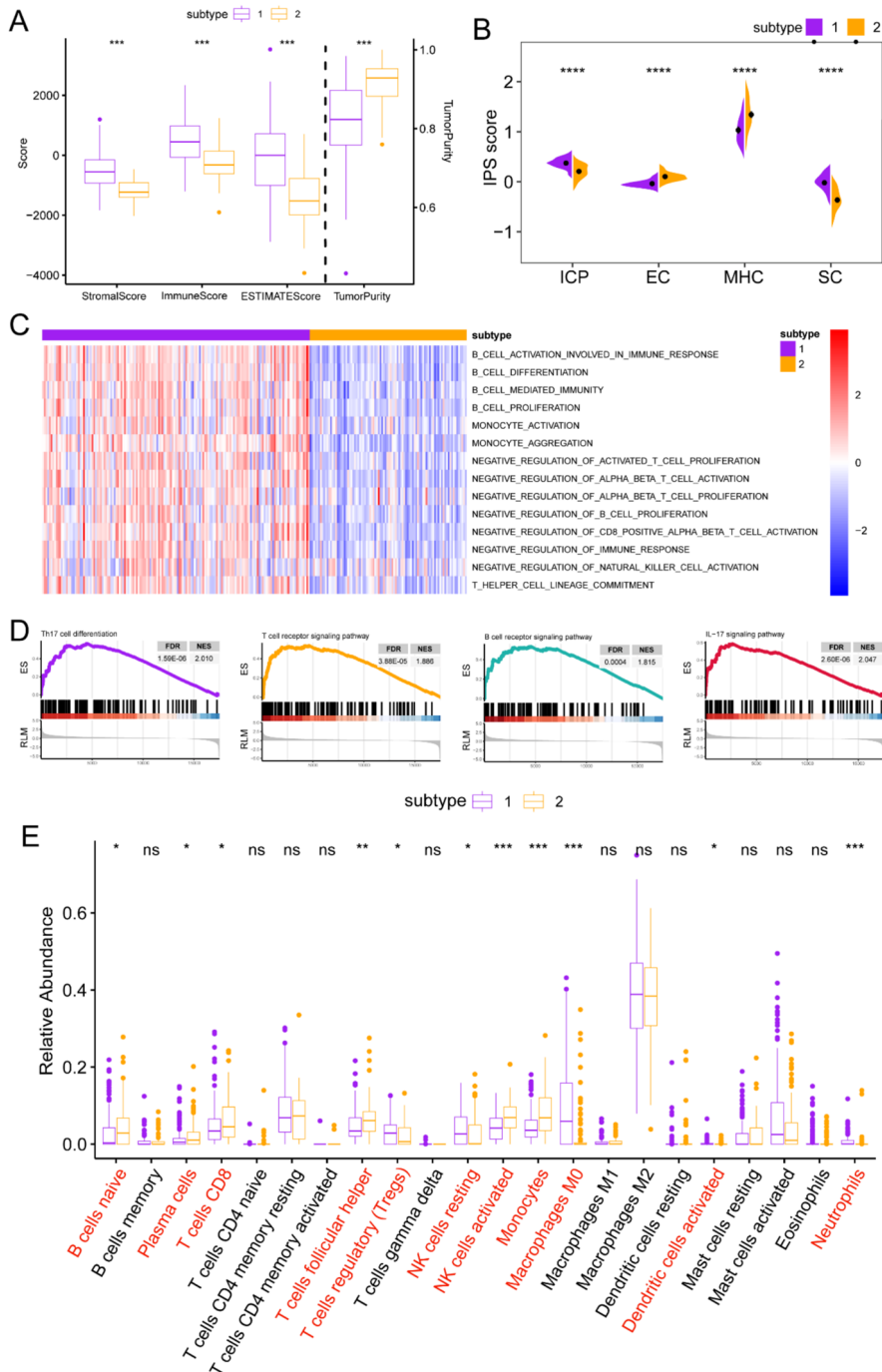
**Fig. 5** Identification of two coagulation-related subtypes in GBM. **A**, clustering heatmap. **B**, the PCA results of the two subtypes. **C**, coagulation scores for individuals across different subtypes. **D**, Kaplan-Meier (KM) curve for individuals of different subtypes. **E**, volcano plot of gene expression between the two subtypes. **F**, heatmap of differentially expressed CRGs

**Fig. 6** Immune infiltration analyses of different subtypes **A**, ESTIMATE results. **B**, IPS results. **C**, GSVA ► results of immune-associated biological processes in different subtypes. **D**, GSEA results showed significant enrichment in immune-associated pathways in different subtypes. **E**, immune cell infiltration landscape between two coagulation-related subtypes. *NES* normalized enrichment score, *IPS* immunophenoscore, *ICP* immune checkpoint, *EC* effector cells, *MHC* major histocompatibility complex molecules, *SC* suppressive cells, *ESTIMATE* The Estimation of Stromal and Immune cells in Malignant Tumor tissues using Expression data, *GSVA* gene set variation analysis, *GSEA* gene set enrichment analysis

a worse prognosis than subtype 2 ( $p=0.0085$ ) (Fig. 5C, D, Supplementary file 3). We used SVM to learn the molecular features of the two subtypes and assign corresponding subtypes to patients in two validation sets. We observed comparable findings in the validation sets, with subtype 1 being associated with a worse prognosis ( $p=0.0024$ ) and a higher coagulation ssGSEA score ( $p<0.0001$ ) (Fig. S1A-S1F, Supplementary file 3). The GSEA results further confirmed that the coagulation pathway was significantly activated in subtype 1 (Figure S1G, Supplementary file 4). Furthermore, we identified a total of 902 DEGs between two subtypes (Fig. 5E, Supplementary file 5), with the expression of DE CRGs in the two subtypes displayed in a heatmap (Fig. 5F).

### Difference in the Immune Landscape Between Two Coagulation-Related GBM Subtypes

To determine the correlation between the coagulation-related subtypes and the immune landscape of GBM, we conducted a series of immune infiltration analyses. The ESTIMATE analysis showed that subtype 1 had a higher ESTIMATE score and lower tumor purity than subtype 2 (Fig. 6A, Fig. S2A). Based on IPS estimation, we found significant differences in immunophenotypes between the two subtypes. Compared to subtype 2, subtype 1 had higher IPS for CP and SC, and lower IPS for EC and MHC, suggesting a suppressive immune microenvironment in subtype 1 (Fig. 6B). Utilizing GSVA and GSEA, we quantified the immune-related pathways between the two subtypes and demonstrated distinct immune infiltrating patterns. The enrichment heatmap illustrated that immune-related biological processes were significantly enriched in subtype 1 (Fig. 6C, Fig. S2B). The results of GSEA showed the DEGs between the two subtypes were enriched in Th17 cell differentiation ( $FDR=1.59E-06$ ,  $NES=2.010$ ), T cell receptor signaling pathway ( $FDR=3.88E-05$ ,  $NES=1.886$ ), B cell receptor signaling pathway ( $FDR=0.0004$ ,  $NES=1.815$ ), and IL-17 signaling pathway ( $FDR=2.60E-06$ ,  $NES=2.047$ ) (Fig. 6D, Fig. S2C-S2D, Supplementary file 6). Considering the significant differences between the two subtypes in the immune landscape, we then explored the TME of the two subtypes by profiling the composition of immune cells with CIBERSORT. The relative abundance of natural killer (NK) cells resting ( $p<0.05$ ) and neutrophil ( $p<0.001$ ) were elevated in subtype 1, while the relative abundance of B cells naïve ( $p<0.05$ ), T cells follicular helper ( $p<0.01$ ), and NK cells activated ( $p<0.001$ ) were elevated in subtype 2, which was consistent across all three datasets (Fig. 6E, Fig. S2E).



## Construction and Validation of a CRG-Based Risk Signature

Survival data from 529 GBM patients in the CGGA693, CGGA325, and TCGA cohorts were systematically analyzed for constructing a CRG-based risk signature. First, we identified 5649 DEGs between the NBT and GBM, including 57 CRGs (Fig. 7A, Supplementary file 7). Among the 57 CRGs, 16 were identified as high-risk factors for GBM patients, and higher expression of these CRGs was associated with a worse prognosis (Fig. 7B). Subsequently, 6 valuable CRGs were selected from 16 prognostic CRGs by LASSO (Fig. 7C). Then 5 CRGs, including CFI (importance = 1.00), GNG12 (importance = 0.85), LEFTY2 (importance = 0.62), MMP2 (importance = 0.43), and SERPINCl (importance = 0.40), were identified as the most valuable CRGs through random survival forest analysis (Fig. 7D, E). The CRGs in the risk signature showed elevated expression in the high-risk group (Fig. 7F). Compared to low-risk patients, high-risk patients had shorter OS ( $p < 0.0001$ ) and were censored earlier (Fig. 7G, H). The AUC of the risk signature in predicting one-, three-, and five-year survival of GBM patients was 0.537, 0.687, and 0.678, respectively (Fig. 7I). The reliability of the risk signature in predicting the prognosis of GBM patients was validated in the CGGA325 and TCGA cohorts. Based on the signature, we calculated the risk score of each patient in the validation sets. Consistent with the results in CGGA693, high-risk patients in CGGA325 and TCGA cohorts had shorter OS and were censored earlier (Fig. S3A-S3F).

## Combination of the Risk Signature and Clinical Characteristics to Construct a Clinical Prediction Model

The relationships between the risk score and key clinical biomarkers of glioma were analyzed. Patients with wildtype IDH ( $p < 0.01$ ) and non-codeletion of 1p/19q ( $p < 0.0001$ ) exhibited higher risk scores (Fig. 8A). The forest plot showed that the risk score ( $p < 0.001$ ), age ( $p = 0.025$ ), IDH mutation status ( $p = 0.004$ ), and 1p/19q codeletion status ( $p = 0.011$ ) were associated with the prognosis of GBM patients (Fig. 8B). Among these clinical characteristics, the 1p/19q codeletion status had the highest coefficient in the multivariate Cox regression model (Fig. 8C). By combining the risk score, age, IDH mutation status, and 1p/19q codeletion status, we constructed a nomogram to enhance the prognostic prediction for GBM patients (Fig. 8D). The calibration curve demonstrated that the predicted survival from the nomogram was a good fit to actual survival (Fig. 8E). The AUC of the nomogram for predicting one-, three-, and five-year survival of GBM patients was 0.740, 0.686, 0.876, respectively (Fig. 8F). We validated the nomogram in the CGGA325 and TCGA cohorts, and the ROC curve of the two validation cohorts also revealed the high predictive power of the nomogram (Fig. S3G-S3J).

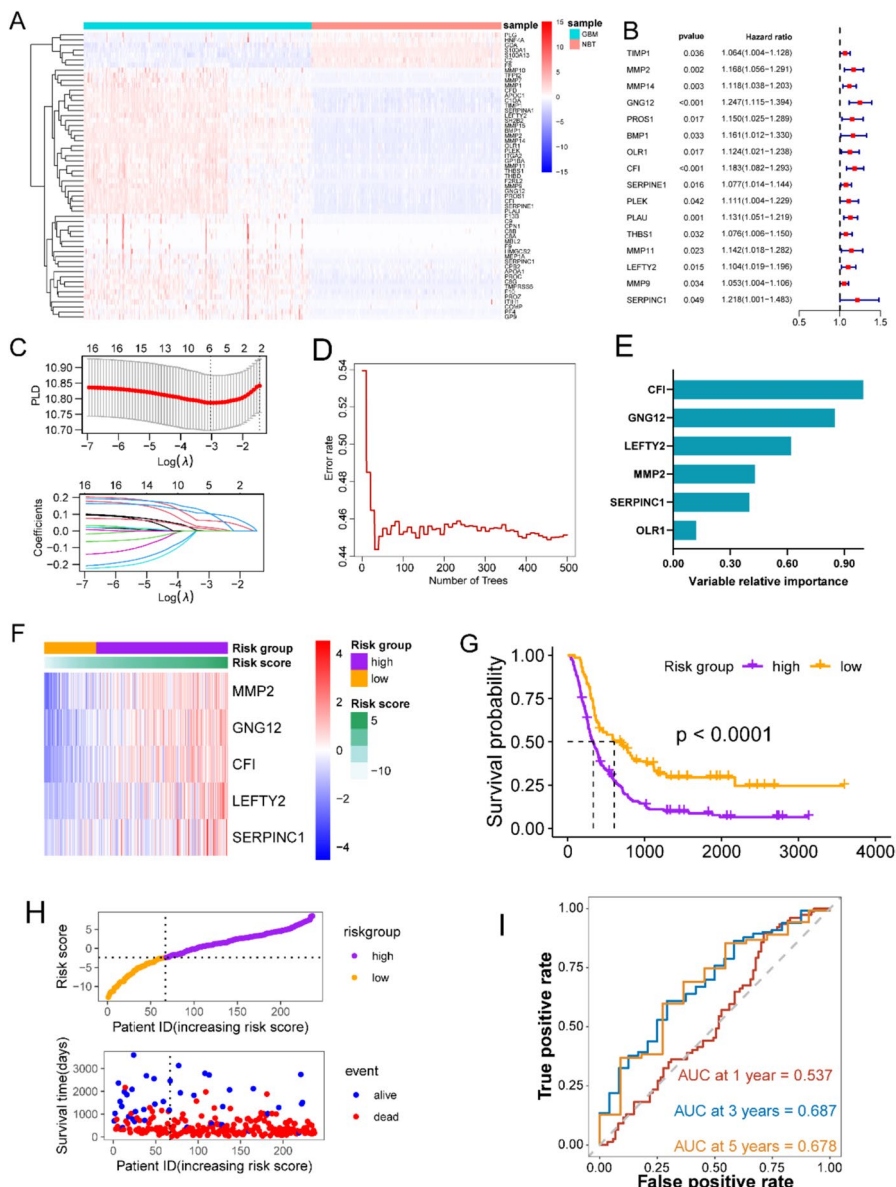


**Fig. 7** Construction of the CRG-based risk signature. **A**, heatmap of DE CRGs between GBM and NBT. **B**, forest plot of DE prognostic CRGs. **C**, LASSO regression analysis to screen prognostic CRGs. **D**, The distribution of error rates in random survival forest. **E**, The variable relative importance of the 6 genes. **F**, expression heatmap of 5 prognostic CRGs. **G**, KM curve of GBM patients in different risk groups. **H**, survival status of GBM patients in different risk groups. **I**, ROC curve of the risk signature. *DE* differentially expressed, *NBT* normal brain tissue

**Fig. 8** Construction of the clinical prediction model based on the risk signature and clinical characteristics. **A**, distribution of risk scores across different clinical characteristics. **B**, forest plot of risk scores and clinical characteristics. **C**, coefficients of risk scores and clinical characteristics in multivariate Cox regression analysis. **D**, nomogram of the clinical prediction model. **E**, calibration curve of the clinical prediction model. **F**, ROC curve of the clinical prediction model. Codel, 1p/19q co-deletion status. Methylated, MGMT promoter Methylation. OS overall survival

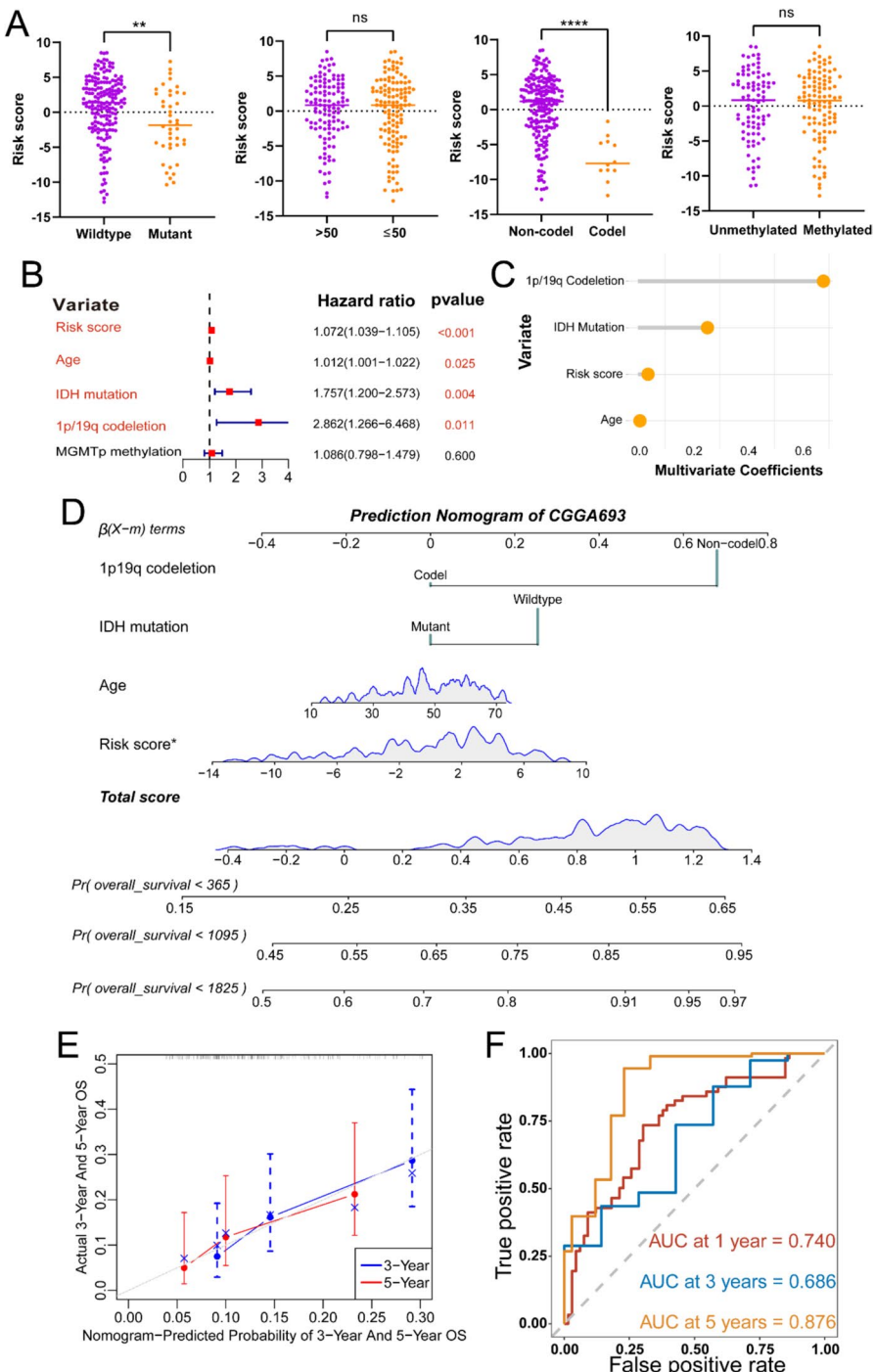
### Predictive Abilities for the Treatment Efficacy of ICI

We compared the expression of several ICPs between the high-risk and low-risk groups. The results demonstrated that the high-risk group had higher expression levels of ICPs than the low-risk group ( $p < 0.01$ ) (Fig. 9A). Compared to the low-risk group, patients in the high-risk group had higher TIDE scores, indicating greater resistance to ICI (Fig. 9B). Based on the risk signature, we calculated the risk scores for patients in three cohorts undergoing ICI treatment. In the IMvigor210 cohort, patients in the high-risk group had shorter OS than those in the low-risk group ( $p = 0.0022$ ) (Fig. 9C). SD/PD patients had higher risk scores ( $p < 0.01$ ), and high-risk patients were also more likely to respond as SD/PD ( $p < 0.05$ ) (Fig. 9D). In two other ICI cohorts, GSE135222 and GSE78220, the risk signature maintained strong predictive ability for forecasting patients' prognosis and their response to ICI (Fig. 9E–H).

### Potential Drugs Predicted Based on the Risk Signature

Using drug sensitivity and expression data, oncoPredict was conducted to estimate the drug sensitivities of GBM patients to hundreds of small molecular drugs. As shown in the flow chart, we performed statistical analyses to identify potential drugs for different risk groups (Fig. 10A). Based on the results of CGGA693 and TCGA, we identified three potential drugs with significantly different sensitivities between high- and low-risk groups (Fig. 10B). From the CTRP2 dataset, 7 drugs were initially identified in the CGGA693 cohort, with 3 overlapping drugs validated in the TCGA cohort: BI2536 ( $p < 0.001$ ), BIBR1532 ( $p < 0.001$ ), and PLX4720 ( $p < 0.01$ ). The correlation analysis revealed a strong association between the risk score and the sensitivities of these three drugs ( $p < 0.001$ ) (Fig. 10C). We then validated the results in the GDSC2 dataset, where the drugs exhibited consistent differences in sensitivity between high- and low-risk groups (Fig. 10D). Among the three drugs, PLX4720 was recommended for treating high-risk patients, because its sensitivity value was negatively correlated with the risk score, indicating high-risk patients respond more sensitively to this drug. The 3D structures of BI2536, BIBR1532, and PLX4720 were obtained from PubChem (Fig. 10E). Taking advantage of three target predicting tools, we further predicted the potential targets of these drugs among the CRGs (Fig. 10F).

Given that PLX4720 was predicted to be effective for the treatment of high-risk patients, we selected it for in vitro validation experiments. CCK8 assays demonstrated that the IC<sub>50</sub> of PLX4720 was  $6.755 \pm 0.322 \mu\text{M}$  in A172 and



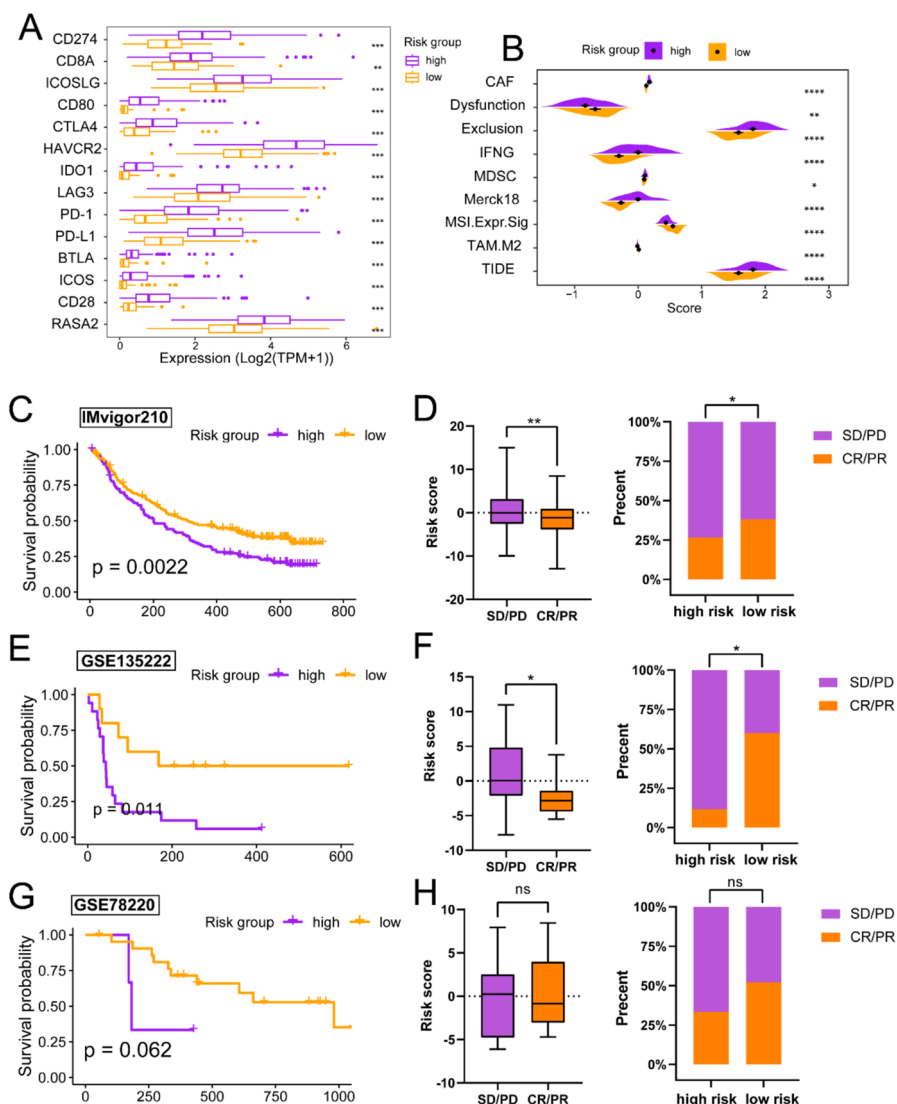


**Fig. 9** The ability of the risk signature to predict the response to immunotherapy. **A**, expression of immune checkpoints in different risk groups. **B**, TIDE analysis results. **C**, KM curve of patients in different risk groups in the IMvigor210 cohort. **D**, boxplot and bar graph of treatment responses to immunotherapy in different risk groups in the IMvigor210 cohort. **E**, **F**, KM curve, boxplot, and bar graph showing treatment responses to immunotherapy in different risk groups in the GSE135222 cohort. **G**, **H**, KM curve, boxplot, and bar graph showing treatment responses to immunotherapy in different risk groups in the GSE78220 cohort. *SD/PD* stable disease or progressive disease, *CR/PR* complete response or partial response, *TPM* Transcripts Per Kilobase of exon model per Million mapped reads, *TIDE* tumor immune dysfunction and exclusion

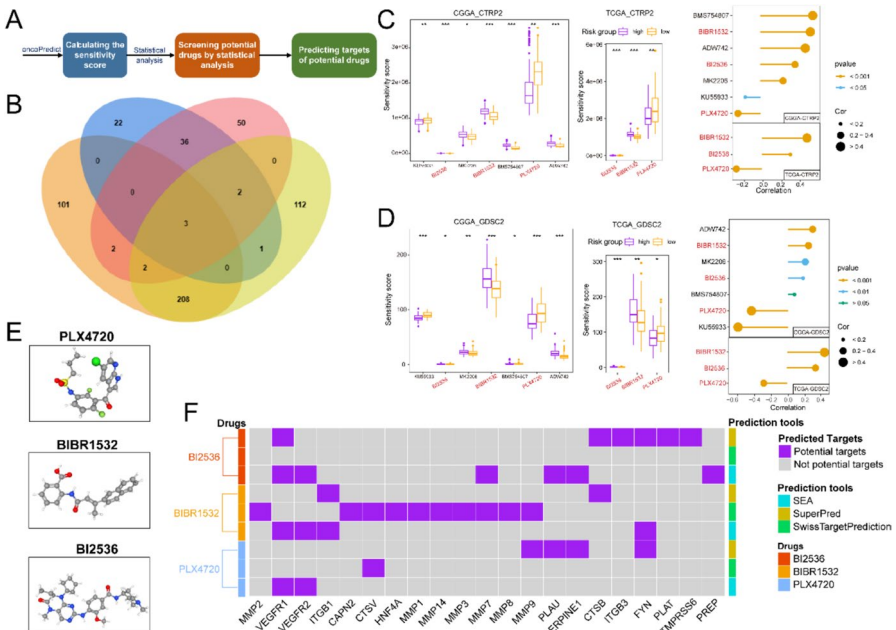


**Fig. 10** Screening potential small-molecule drugs based on the risk signature **A**, flow chart for screening potential drugs. **B**, Venn diagram of predicted drugs. **C**, screening of potential drugs based on the CTRP database. **D**, screening of potential drugs based on the GDSC database. **E**, 3D structural models of three potential small-molecule drugs. **F**, heatmap showing the predicted CRG targets of the potential drugs based on three databases. *CTRP* the Cancer Therapeutics Response Portal, *GDSC* the Genomics of Drug Sensitivity in Cancer database

$6.560 \pm 0.623 \mu\text{M}$  in U251 cells (Fig. 11A). At a concentration of  $6 \mu\text{M}$ , PLX4720 significantly reduced the viability of both A172 and U251 cells compared to the control group ( $p < 0.0001$ ), indicating its ability to inhibit glioma cell proliferation (Fig. 11B). Wound healing assays showed that after 48 h, the wound area of the dosing group was significantly larger than that of the control group ( $p < 0.0001$ ), and PLX4720 was able to inhibit the migration ability of glioma cells (Fig. 11C, D). Colony formation assays demonstrated that after 14 days, significantly fewer colonies were observed in the dosing group compared to the control group ( $p < 0.0001$ ), confirming that PLX4720 effectively inhibits long-term glioma cell proliferation (Fig. 11E, F).

## In Vitro Experiments to Validate the Role of LEFTY2 and SERPINC1 in Glioma Cells

We selected LEFTY2 and SERPINC1, which had not been reported before, and performed a series of experiments to validate their roles in GBM. We assessed the expression differences of LEFTY2 and SERPINC1 between GBM and NBT using immunohistochemistry and found that both LEFTY2 ( $p < 0.05$ ) and SERPINC1 ( $p < 0.01$ ) were highly expressed in GBM (Fig. 12A, B). To explore their functional

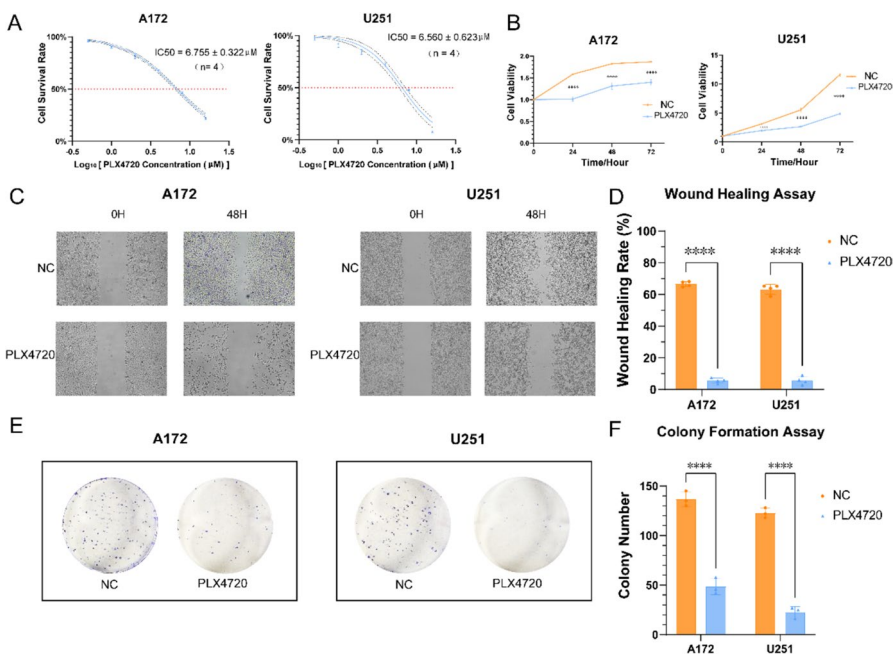


**Fig. 11** Drug experimental validation of PLX4720 **A**, Dose–response curves and IC<sub>50</sub> of PLX4720 in A172 and U251 cells. **B**, Cell proliferation curves demonstrating cell viability. **C**, Results of wound healing experiment. **D**, Wound healing rate in the 48 h dosing group and the control group. **E**, Results of colony formation assay. **F**, The number of colonies in the dosing group and the control group after 14 days. NC negative control

impact of LEFTY2 and SERPINC1 in GBM cells, we further knocked down LEFTY2 and SERPINC1 in the A172 and U251 cell lines (Fig. 12C). CCK-8 and wound healing assays were conducted with A172 and U251 cells in which LEFTY2 and SERPINC1 were knocked down. The results of the CCK-8 assay showed that the knockdown of LEFTY2 and SERPINC1 attenuated the proliferation of A172 and U251 cells ( $p < 0.0001$ ) (Fig. 12D). The wound healing assay demonstrated that cell migratory capacity was significantly reduced with lower expression of LEFTY2 and SERPINC1 in A172 and U251 cells ( $p < 0.05$ ) (Fig. 12E, F).

## Discussion

In previous studies, Ming Cao et al. utilized RNA-seq data from GBM and LGG patients in the TCGA and CGGA databases to construct prognostic models (Cao et al. 2024). Similarly, Min Zhou et al. analyzed RNA-seq data from GBM patients in the TCGA and CGGA databases, identified differentially expressed CRGs, and established prognostic signatures, highlighting the potential role of CRGs in GBM progression (Zhou et al. 2023). In this study, we comprehensively analyzed single nucleotide polymorphism and copy number variation data, RNA-seq data and scRNA-seq data. Through cellular network communication analysis, we

identified the key role of the SPP1-Integrin pathway in driving GBM invasiveness, a finding reported here for the first time. Two coagulation-associated subtypes and the immune microenvironmental differences between the two in patients with GBM were identified by clustering analysis and ssGSEA scores. The newly identified LEFTY2 and SERPINC1 were validated *in vitro* to demonstrate their expression levels in GBM and normal brain tissues and their roles in regulating the proliferation and migration of GBM. Moreover, a series of experimental validations were performed on the potential drug PLX4720 to demonstrate its potential for the treatment of GBM patients.

Coagulation in GBM significantly influences both gene expression levels and the TME (Saidak et al. 2021; Yerrabothala et al. 2021; Anand and Brat 2012). By analyzing scRNA-seq data, we investigated the molecular mechanisms of coagulation in GBM, focusing specifically on the role of endothelial cells in its regulation. Healthy endothelial cells play a key role in preventing coagulation and thrombosis by expressing anticoagulant proteins (Bochenek and Schafer 2019). However, in GBM, dysfunctional endothelial cells may promote thrombosis by increasing the expression of adhesion receptors and tissue factors (Iba and Levy 2018; Poll and Parker 2020; Goldman et al. 1993). Our study found that the coagulation process in GBM was predominantly active in endothelial cells, indicating a strong association between coagulation and endothelial cells within the TME of GBM. Correlation and communication network analyses revealed that coagulation activation in GBM endothelial cells was associated with the SPP1-integrin pathway. SPP1 has previously been identified as a candidate biomarker for deep vein thrombosis (Memon et al. 2018), and integrins regulate coagulation factor activity through direct interactions (Kocaturk and Versteeg 2013). Endothelial cells may interact with other cells through the SPP1-integrin signaling pathway, thus facilitating coagulation activation. These findings shed light on the potential mechanisms of coagulation in the GBM microenvironment and suggest that coagulation may regulate the evolution of the TME through communication networks involving endothelial cells and other cell types.

This study identified two novel coagulation-related subtypes in GBM patients through clustering analysis and ssGSEA scoring: a coagulation-activated subtype and a coagulation-inhibited subtype. Immune infiltration analysis revealed differences in the immune microenvironment between the two subtypes. Compared to the coagulation-inhibited subtype, patients in the coagulation-activated subtype had lower tumor purity and greater infiltration of immune suppressive cells. Notably, natural killer (NK) cells exhibited a dormant state in the coagulation-activated group but demonstrated activation in the coagulation-inhibited group. The activation of NK cells significantly enhances their antitumor capacity (Shimasaki et al. 2020), leading to prolonged survival in GBM patients with the coagulation-inhibited subtype. Moreover, major histocompatibility complex (MHC) molecules were downregulated in the coagulation-activated subtype and upregulated in the coagulation-inhibited subtype. Tumor cells often evade CD8 T-cell-mediated cytotoxicity by downregulating MHC class I molecules (Wu et al. 2020). This suggests that the coagulation-activated subtype has a stronger immune evasion capacity than the coagulation-inhibited

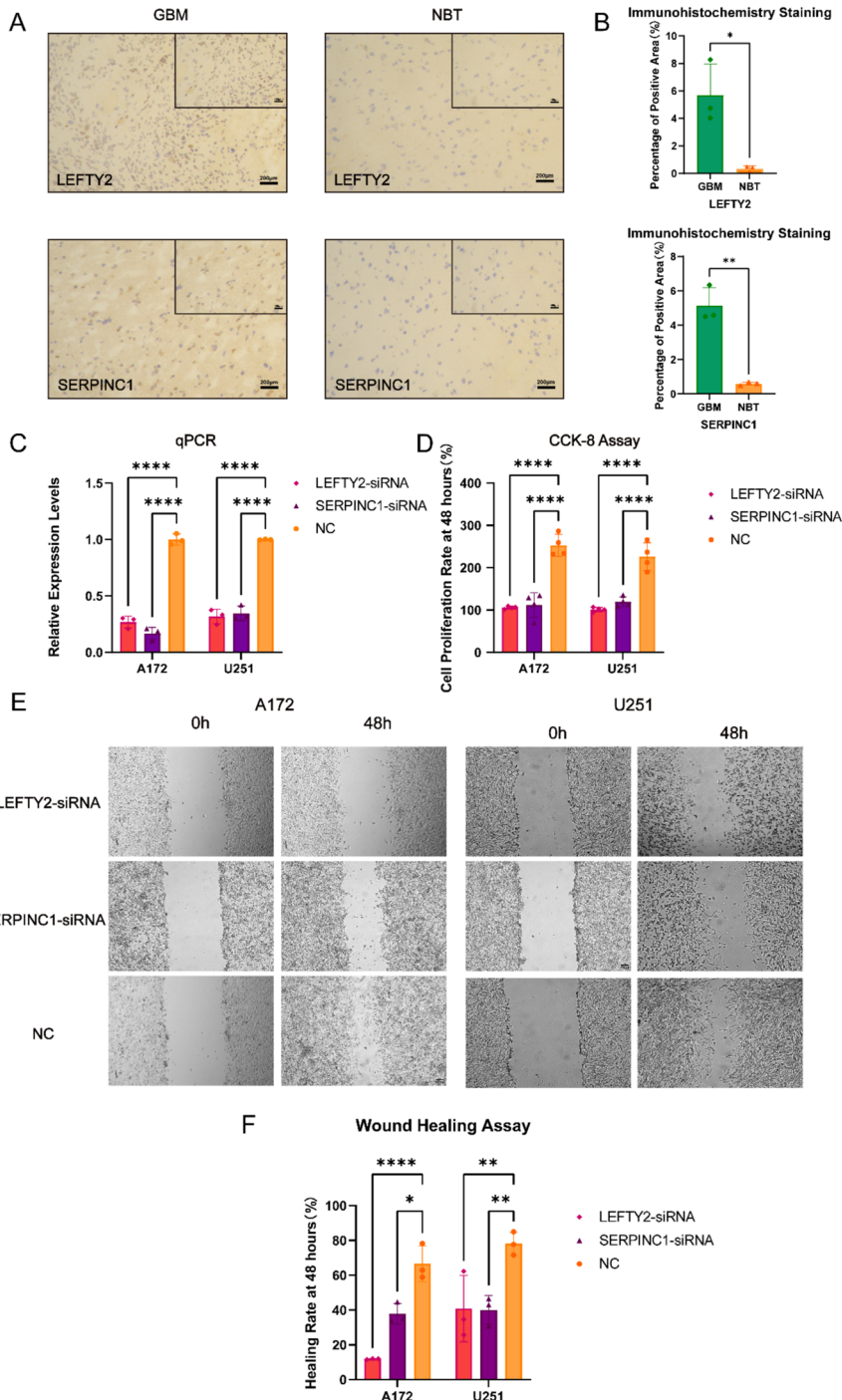
**Fig. 12** In vitro experimental validation of LEFTY2 and SERPINC1. **A**, Immunohistochemical staining. ▶ **B**, expression levels of LEFTY2 and SERPINC1 in GBM and NBT. **C**, qPCR to verify the knockdown efficiency of LEFTY2 and SERPINC1. **D**, results of the CCK8 assay. **E**, results of the wound healing assay. **F**, wound healing rate at 48 h after knockdown of LEFTY2 and SERPINC1 in A172 and U251 cells. *GBM* glioblastoma tissue, *NBT* normal brain tissue

subtype, which may be associated with shorter OS and worse prognosis. These findings highlight the importance of the immune microenvironment in different coagulation subtypes and provide a basis for further research into the interaction between coagulation and the immune system in GBM.

Among the 3 drugs we identified, BI2536 is a PLK1 inhibitor and has demonstrated efficacy in promoting apoptosis in GBM cells (Wang et al. 2020; Pezuk et al. 2013). BIBR1532, a telomerase inhibitor, promotes GBM cell death through epigenetic mechanisms (Biray et al. 2018). The BRAF mutation V600E is critical in a small proportion of GBM cases (Dasgupta et al. 2016). PLX4720 is a BRAF (V600E)-specific inhibitor, and studies have demonstrated that PLX4720 is a potential radiosensitizer for GBM (Fan et al. 2023). After further drug validation experiments with PLX4720, which was predicted to be effective in the treatment of high-risk patients, we confirmed that PLX4720 possesses the ability to inhibit the proliferation and migration of glioma cells. This not only proves the reliability of our prediction, but also identifies the potential of PLX4720 in the treatment of GBM.

Using machine learning and bioinformatic analyses, this study identified five key CRGs from multiple databases, including CFI, GNG12, MMP2, LEFTY2, and SERPINC1. These five genes play critical roles in GBM progression and are closely associated with patient prognosis. While the roles of CFI (Cai et al. 2020), GNG12 (Liu et al. 2022), and MMP2 (Zhou et al. 2019) in GBM have been previously reported, the functions of LEFTY2 and SERPINC1 in GBM remain unclear. In this study, we validated their functions through in vitro experiments, demonstrating that LEFTY2 and SERPINC1 were significantly overexpressed in GBM and promoted glioma cell proliferation and migration. The knockdown of these genes inhibited glioma cell proliferation and migration. This discovery not only broadens our understanding of the biological functions of CRGs in GBM but also lays the groundwork for further studies on the specific molecular mechanisms of these CRGs in GBM.

However, there are still some limitations of this study. First, this study only focused on CRGs and did not fully consider other key genes that may affect prognosis. Second, the clinical data in the public dataset were more limited and lacked comprehensive clinical background information, which may have biased the results of the study to some extent. In addition, although the CRG-based risk signature model showed some predictive ability, its accuracy still needs to be further validated by more *in vivo* and *in vitro* experiments. Future studies should focus on elucidating the molecular mechanisms of these key CRGs and exploring in depth their biological functions in coagulation-activated and coagulation-inhibited subtypes of GBM. With the introduction of more clinical data and enhanced experimental validation, the current risk model is expected to



be optimized to provide more precise and personalized therapeutic strategies for GBM patients.

## Conclusion

This study identified two coagulation-related subtypes in GBM and uncovered the role of coagulation in GBM progression. In the TME, thrombosis and coagulation-related oncological effects are closely associated with the interactions between GBM cells and endothelial cells. The CRG-based risk signature model effectively predicted patient prognosis and the efficacy of ICI treatment and chemotherapy. Furthermore, the newly identified genes LEFTY2 and SERPINC1, as well as the drug PLX4720 provide valuable insights for the development of novel therapeutic strategies for GBM in clinical practice.

**Supplementary Information** The online version contains supplementary material available at <https://doi.org/10.1007/s10528-025-11086-3>.

**Acknowledgements** Not applicable.

**Author Contributions** S.S.C. and N.X.X. conceived, designed, and supervised the study., J.Y.Y., L.S. and Y.K.C. drafted the manuscript and conducted validation experiments. K.Y.C. and D.Y.X. collected the data. Y.L., and J.W. performed data analysis and visualization. All authors contributed to the article and approved the submitted version.

**Funding** This study did not receive any funding.

**Data Availability** The datasets CGGA693 and CGGA325 can be found in the GDSC database (<http://www.cggta.org.cn/download.jsp>). The genomic data of GBM in TCGA and normal brain tissue in GTEx can be found in the UCSC Xena database (<https://xenabrowser.net/datapages/>). The datasets IMvigor210 can be found in the R package IMvigor210CoreBiologies (<http://research-pub.gene.com/IMvigor210CoreBiologies/>). The datasets GSE141383, GSE135222, and GSE78220 can be found in the GEO database (<https://www.ncbi.nlm.nih.gov/geo/>). The dataset GDSC2 can be found in the GDSC database (<https://www.cancerrxgene.org/>). The dataset CTRP v2 can be found in the CTRP database (<https://portals.broadinstitute.org/ctrp/>).

## Declarations

**Competing interest** The authors declare no competing interests.

**Ethical Approval and Consent to Participate** The current study was performed in accordance with the Declaration of Helsinki. This study was approved by the Medical Ethics Committee of Wuhan University Central South Hospital (Ethical Approval No. 2021080) and written informed consent was obtained from the patients.

**Consent for Publication** Not applicable.

## References

- Aibar S, Gonzalez-Blas CB, Moerman T, Huynh-Thu VA, Imrichova H, Hulselmans G et al (2017) SCE-NIC: single-cell regulatory network inference and clustering. Nat Methods 14(11):1083–1086

- Aleksander SA, Balhoff J, Carbon S, Cherry JM, Drabkin HJ, Ebert D et al (2023) The gene ontology knowledgebase in 2023. *Genetics* 224(1):iyad031
- Alexander BM, Cloughesy TF (2017) Adult glioblastoma. *J Clin Oncol* 35(21):2402–2409
- Anand M, Brat DJ (2012) Oncogenic regulation of tissue factor and thrombosis in cancer. *Thromb Res* 129(Suppl 1):S46–S49
- Andreatta M, Carmona SJ (2021) UCell: Robust and scalable single-cell gene signature scoring. *Comput Struct Biotechnol* 19:3796–3798
- Barretina J, Caponigro G, Stransky N, Venkatesan K, Margolin AA, Kim S et al (2012) The cancer cell line encyclopedia enables predictive modelling of anticancer drug sensitivity. *Nature* 483(7391):603–607
- Bauer AT, Gorzelanny C, Gebhardt C, Pantel K, Schneider SW (2022) Interplay between coagulation and inflammation in cancer: Limitations and therapeutic opportunities. *Cancer Treat Rev* 102:102322
- Biray AC, Dogan F, Ozates AN, Goker BB, Abbaszadeh Z, Gunduz C (2018) Effects of telomerase inhibitor on epigenetic chromatin modification enzymes in malignancies. *J Cell Biochem* 119(12):9817–9824
- Bochenek ML, Schafer K (2019) Role of endothelial cells in acute and chronic thrombosis. *Hamostaseologie* 39(2):128–139
- Brat DJ, Van Meir EG (2004) Vaso-occlusive and prothrombotic mechanisms associated with tumor hypoxia, necrosis, and accelerated growth in glioblastoma. *Lab Invest* 84(4):397–405
- Cai X, Qiu W, Qian M, Feng S, Peng C, Zhang J et al (2020) A candidate prognostic biomarker complement factor i promotes malignant progression in glioma. *Front Cell Dev Biol* 8:615970
- Cao M, Chen J, Guo RZ (2024) Evaluating the predictive value of a coagulation-related gene model in glioma. *Turk Neurosurg* 34(4):708–715
- Chen AX, Gartrell RD, Zhao J, Upadhyayula PS, Zhao W, Yuan J et al (2021) Single-cell characterization of macrophages in glioblastoma reveals MARCO as a mesenchymal pro-tumor marker. *Genome Med* 13(1):88
- Dasgupta T, Olow AK, Yang X, Hashizume R, Nicolaides TP, Tom M et al (2016) Survival advantage combining a BRAF inhibitor and radiation in BRAF V600E-mutant glioma. *J Neuro-Oncol* 126(3):385–393
- Falanga A, Marchetti M, Vignoli A (2013) Coagulation and cancer: biological and clinical aspects. *J Thromb Haemost* 11(2):223–233
- Falanga A, Marchetti M, Russo L (2021) Hemostatic biomarkers and cancer prognosis: where do we stand? *Semin Thromb Hemost* 47(8):962–971
- Fan Y, Gao Z, Xu J, Wang H, Guo Q, Li B et al (2023) SPI1-mediated MIR222HG transcription promotes proneural-to-mesenchymal transition of glioma stem cells and immunosuppressive polarization of macrophages. *Theranostics* 13(10):3310–3329
- Foroutan M, Bhuvu DD, Lynn R, Horan K, Cursons J, Davis MJ (2018) Single sample scoring of molecular phenotypes. *BMC Bioinform* 19(1):404
- Gfeller D, Michielin O, Zoete V (2013) Shaping the interaction landscape of bioactive molecules. *Bioinformatics* 29(23):3073–3079
- Goldman CK, Kim J, Wong WL, King V, Brock T, Gillespie GY (1993) Epidermal growth factor stimulates vascular endothelial growth factor production by human malignant glioma cells: a model of glioblastoma multiforme pathophysiology. *Mol Biol Cell* 4(1):121–133
- GTEx Consortium (2013) The Genotype-Tissue Expression (GTEx) project. *Nat Genet* 45(6):580–585
- Hanzelmann S, Castelo R, Guinney J (2013) GSVA: gene set variation analysis for microarray and RNA-seq data. *BMC Bioinform* 14:7
- He Q, Yang J, Jin Y (2022) Immune infiltration and clinical significance analyses of the coagulation-related genes in hepatocellular carcinoma. *Brief Bioinform*. <https://doi.org/10.1093/bib/bbac291>
- Hugo W, Zaretsky JM, Sun L, Song C, Moreno BH, Hu-Lieskován S et al (2016) Genomic and transcriptomic features of response to anti-PD-1 therapy in metastatic melanoma. *Cell* 165(1):35–44
- Iba T, Levy JH (2018) Inflammation and thrombosis: roles of neutrophils, platelets and endothelial cells and their interactions in thrombus formation during sepsis. *J Thromb Haemost* 16(2):231–241
- Jiang P, Gu S, Pan D, Fu J, Sahu A, Hu X et al (2018) Signatures of T cell dysfunction and exclusion predict cancer immunotherapy response. *Nat Med* 24(10):1550–1558
- Jin S, Guerrero-Juarez CF, Zhang L, Chang I, Ramos R, Kuan CH et al (2021) Inference and analysis of cell-cell communication using Cell Chat. *Nat Commun* 12(1):1088
- Jung H, Kim HS, Kim JY, Sun JM, Ahn JS, Ahn MJ et al (2019) DNA methylation loss promotes immune evasion of tumours with high mutation and copy number load. *Nat Commun* 10(1):4278

- Kanehisa M, Furumichi M, Sato Y, Ishiguro-Watanabe M, Tanabe M (2021) KEGG: integrating viruses and cellular organisms. *Nucleic Acids Res* 49(D1):D545–D551
- Keiser MJ, Roth BL, Armbruster BN, Ernsberger P, Irwin JJ, Shoichet BK (2007) Relating protein pharmacology by ligand chemistry. *Nat Biotechnol* 25(2):197–206
- Khasraw M, Fujita Y, Lee-Chang C, Balyasnikova IV, Najem H, Heimberger AB (2022) New approaches to glioblastoma. *Annu Rev Med* 73:279–292
- Kim S, Chen J, Cheng T, Gindulyte A, He J, He S et al (2021) PubChem in 2021: new data content and improved web interfaces. *Nucleic Acids Res* 49(D1):D1388–D1395
- Kocaturk B, Versteeg HH (2013) Tissue factor-integrin interactions in cancer and thrombosis: every Jack has his Jill. *J Thromb Haemost* 11(Suppl 1):285–293
- Kolde R, Laur S, Adler P, Vilo J (2012) Robust rank aggregation for gene list integration and meta-analysis. *Bioinformatics* 28(4):573–580
- Korsunsky I, Millard N, Fan J, Slowikowski K, Zhang F, Wei K et al (2019) Fast, sensitive and accurate integration of single-cell data with Harmony. *Nat Methods* 16(12):1289–1296
- Li Y, Ge X, Peng F, Li W, Li JJ (2022) Exaggerated false positives by popular differential expression methods when analyzing human population samples. *Genome Biol* 23(1):79
- Liberzon A, Birger C, Thorvaldsdottir H, Ghandi M, Mesirov JP, Tamayo P (2015) The molecular signatures database (MSigDB) hallmark gene set collection. *Cell Syst* 1(6):417–425
- Liu R, Liu Z, Zhao Y, Cheng X, Liu B, Wang Y et al (2022) GNG12 as a novel molecular marker for the diagnosis and treatment of glioma. *Front Oncol* 12:726556
- Maeser D, Gruener RF, Huang RS (2021) oncoPredict: an R package for predicting in vivo or cancer patient drug response and biomarkers from cell line screening data. *Brief Bioinform*. <https://doi.org/10.1093/bib/bbab260>
- Magnus N, D'Asti E, Garnier D, Meehan B, Rak J (2013a) Brain neoplasms and coagulation. *Semin Thromb Hemost* 39(8):881–895
- Magnus N, Gerges N, Jabado N, Rak J (2013b) Coagulation-related gene expression profile in glioblastoma is defined by molecular disease subtype. *J Thromb Haemost* 11(6):1197–1200
- Magnus N, D'Asti E, Meehan B, Garnier D, Rak J (2014) Oncogenes and the coagulation system—forces that modulate dormant and aggressive states in cancer. *Thromb Res* 133(Suppl 2):S1–S9
- McKinnon C, Nandhabalan M, Murray SA, Plaha P (2021) Glioblastoma: clinical presentation, diagnosis, and management. *BMJ* 374:n1560
- Memon AA, Sundquist K, PirouziFard M, Elf JL, Strandberg K, Svensson PJ et al (2018) Identification of novel diagnostic biomarkers for deep venous thrombosis. *Brit J Haematol* 181(3):378–385
- Mermel CH, Schumacher SE, Hill B, Meyerson ML, Beroukhim R, Getz G (2011) GISTIC2.0 facilitates sensitive and confident localization of the targets of focal somatic copy-number alteration in human cancers. *Genome Biol* 12(4):R41
- Necchi A, Joseph RW, Loriot Y, Hoffman-Censits J, Perez-Gracia JL, Petrylak DP et al (2017) Atezolizumab in platinum-treated locally advanced or metastatic urothelial carcinoma: post-progression outcomes from the phase II IMVigor210 study. *Ann Oncol* 28(12):3044–3050
- Neftel C, Laffy J, Filbin MG, Hara T, Shore ME, Rahme GJ et al (2019) An integrative model of cellular states, plasticity, and genetics for glioblastoma. *Cell* 178(4):835–849
- Newman AM, Liu CL, Green MR, Gentles AJ, Feng W, Xu Y et al (2015) Robust enumeration of cell subsets from tissue expression profiles. *Nat Methods* 12(5):453–457
- Nickel J, Gohlke BO, Erehman J, Banerjee P, Rong WW, Goede A et al (2014) SuperPred: update on drug classification and target prediction. *Nucleic Acids Res*. <https://doi.org/10.1093/nar/gku477>
- Pezuk JA, Brassesco MS, Morales AG, de Oliveira JC, de Paula QR, Machado HR et al (2013) Polo-like kinase 1 inhibition causes decreased proliferation by cell cycle arrest, leading to cell death in glioblastoma. *Cancer Gene Ther* 20(9):499–506
- Prayson NF, Koch P, Angelov L, Prayson RA (2011) Microscopic thrombi in anaplastic astrocytoma predict worse survival? *Ann Diagn Pathol* 15(6):389–393
- Qazi MA, Vora P, Venugopal C, Sidhu SS, Moffat J, Swanton C et al (2017) Intratumoral heterogeneity: pathways to treatment resistance and relapse in human glioblastoma. *Ann Oncol* 28(7):1448–1456
- Rees MG, Seashore-Ludlow B, Cheah JH, Adams DJ, Price EV, Gill S et al (2016) Correlating chemical sensitivity and basal gene expression reveals mechanism of action. *Nat Chem Biol* 12(2):109–116
- Repetto O, De Re V (2017) Coagulation and fibrinolysis in gastric cancer. *Ann NY Acad Sci* 1404(1):27–48
- Rong L, Li N, Zhang Z (2022) Emerging therapies for glioblastoma: current state and future directions. *J Exp Clin Canc Res* 41(1):142

- Saidak Z, Soudet S, Lottin M, Salle V, Sevestre MA, Clatot F et al (2021) A pan-cancer analysis of the human tumor coagulome and its link to the tumor immune microenvironment. *Cancer Immunol Immun* 70(4):923–933
- Satija R, Farrell JA, Gennert D, Schier AF, Regev A (2015) Spatial reconstruction of single-cell gene expression data. *Nat Biotechnol* 33(5):495–502
- Shimasaki N, Jain A, Campana D (2020) NK cells for cancer immunotherapy. *Nat Rev Drug Discov* 19(3):200–218
- Subramanian A, Tamayo P, Mootha VK, Mukherjee S, Ebert BL, Gillette MA et al (2005) Gene set enrichment analysis: a knowledge-based approach for interpreting genome-wide expression profiles. *Proc Natl Acad Sci U S A* 102(43):15545–15550
- Taylor JM (2011) Random survival forests. *J Thorac Oncol* 6(12):1974–1975
- Tehrani M, Friedman TM, Olson JJ, Brat DJ (2008) Intravascular thrombosis in central nervous system malignancies: a potential role in astrocytoma progression to glioblastoma. *Brain Pathol* 18(2):164–171
- Tibshirani R (1997) The lasso method for variable selection in the Cox model. *Stat Med* 16(4):385–395
- van der Poll T, Parker RI (2020) Platelet activation and endothelial cell dysfunction. *Crit Care Clin* 36(2):233–253
- Wang H, Tao Z, Feng M, Li X, Deng Z, Zhao G et al (2020) Dual PLK1 and STAT3 inhibition promotes glioblastoma cells apoptosis through MYC. *Biochem Bioph Res Commun* 533(3):368–375
- Wilkerson MD, Hayes DN (2010) ConsensusClusterPlus: a class discovery tool with confidence assessments and item tracking. *Bioinformatics* 26(12):1572–1573
- Wu SY, Fu T, Jiang YZ, Shao ZM (2020) Natural killer cells in cancer biology and therapy. *Mol Cancer* 19(1):120
- Yang W, Soares J, Greninger P, Edelman EJ, Lightfoot H, Forbes S et al (2013) Genomics of Drug Sensitivity in Cancer (GDSC): a resource for therapeutic biomarker discovery in cancer cells. *Nucleic Acids Res.* <https://doi.org/10.1093/nar/gks1111>
- Yerrabothala S, Gourley BL, Ford JC, Ahmed SR, Guerin SJ, Porter M et al (2021) Systemic coagulation is activated in patients with meningioma and glioblastoma. *J Neuro-Oncol* 155(2):173–180
- Yoshihara K, Shahmoradgoli M, Martinez E, Vegesna R, Kim H, Torres-Garcia W et al (2013) Inferring tumour purity and stromal and immune cell admixture from expression data. *Nat Commun* 4:2612
- Zhou W, Yu X, Sun S, Zhang X, Yang W, Zhang J et al (2019) Increased expression of MMP-2 and MMP-9 indicates poor prognosis in glioma recurrence. *Biomed Pharmacother* 118:109369
- Zhou M, Deng Y, Fu Y, Liang R, Liu Y, Liao Q (2023) A new prognostic model for glioblastoma multiforme based on coagulation-related genes. *Transl Cancer Res* 12(10):2898–2910

**Publisher's Note** Springer Nature remains neutral with regard to jurisdictional claims in published maps and institutional affiliations.

Springer Nature or its licensor (e.g. a society or other partner) holds exclusive rights to this article under a publishing agreement with the author(s) or other rightholder(s); author self-archiving of the accepted manuscript version of this article is solely governed by the terms of such publishing agreement and applicable law.

## Authors and Affiliations

Jingyi Yang<sup>1</sup> · Lei Shen<sup>1</sup> · Yuankun Cai<sup>1</sup> · Ji Wu<sup>1</sup> · Keyu Chen<sup>1</sup> · Dongyuan Xu<sup>1</sup> ·  
Yu Lei<sup>1</sup> · Songshan Chai<sup>1</sup> · Nanxiang Xiong<sup>1</sup>

✉ Songshan Chai  
chai\_s\_s@qq.com

✉ Nanxiang Xiong  
mozhuoxiong@163.com

<sup>1</sup> Department of Neurosurgery, Zhongnan Hospital of Wuhan University, Donghu Road 169,  
Wuhan 430071, China